AGU
ADVANCING EARTH AND SPACE SCIENCE

# Tectonics®

**Key Points:**

- The 2015 Sarez earthquake unlocked the Aramkungey fault at 150 km distance but in the following 0.5–2.5 years the locking began again
- 10–20 mm Alai coseismic displacements toward the Sarez earthquake epicenter led to a slight decrease in the load state of this area
- The Sarez coseismic deformations attenuated faster in the decompaction strip around the Aramkungey fault with a width of at least 7.5 km

# Cyclic Fault Slip Under the Magnifier: Co- and Postseismic Response of the Pamir Front to the 2015 $M_w$7.2 Sarez, Central Pamir, Earthquake

**A. Zubovich[1]** [ID]**, S. Metzger[2]** [ID] **, T. Schöne[2], J. Kley[3]** [ID] **, O. Mosienko[1], C. Zech[2], B. Moldobekov[1], and A. Shsarshebaev[1]**

[1]Central-Asian Institute for Applied Geosciences, Bishkek, Kyrgyzstan, [2]Helmholtz Centre Potsdam, GFZ German Research Centre for Geosciences, Potsdam, Germany, [3]Georg-August-University Göttingen, Geoscience Centre, Structural Geology & Geodynamics, Göttingen, Germany

**Abstract** The constant increase of geodetic instrumentation over the past decades enables us to not only detect ever smaller tectonic signals but also to monitor their evolution in time and space. We present spatial and temporal slip variations observed on a fault affected by a large, intermediate-field earthquake: the 2015 $M_w$7.2 Sarez, Central Pamir, earthquake ruptured the sinistral, NE-trending Sarez-Karakul fault system. 120–170 km North of the main rupture, the thin-skinned, E-trending Pamir thrust system bounding the Pamir to the North was co-seismically activated. We derived co-seismic offsets and post-seismic rates observed by two dense, high-rate Global Positioning System (GPS) profiles crossing the Pamir thrust system at different longitudes. The continuous GPS observations of the western profile focus on the dextral, NW-striking Aramkungey fault segment that connects two thrust faults with opposite dip. We compare inter-, co- and post-seismic displacement rates by complementing the continuous data with survey-mode GPS data and East rates derived from satellite radar interferometric displacement time-series. All the GPS stations were shifted toward the epicenter against the direction of the interseismic load with an increased gradient in the Aramkungey fault segment. During the postseismic stage, the fault-parallel and fault-perpendicular rates were affected differently, suggesting gradual re-locking of the Aramkungey fault after its unlocking by right-lateral co-seismic slip.

**Plain Language Summary** The 2015 $M_w$7.2 Sarez earthquake, occurred in the Central Pamir, caused m-scale displacement of the Earth's surface. This earthquake also affected another system near the northern Pamir front at 120–170 km distance from the epicenter where the Pamir thrust system separates the Pamir from the Alay valley (a testimony of an ancient ocean) and the adjacent Tien Shan mountain range to the North. Time-series analysis of accurate positioning data (GPS) showed 10–20 mm displacements of the Alai crust surface toward the earthquake epicenter with an increased level of deformation near the western segment of the system—in the zone of the Aramkungey right strike-slip fault. As a result of the earthquake, this fault was unlocked, but then gradually began to be relocked, accelerating the strain accumulation in the following 4.5 years.

## 1. Introduction

It is generally assumed that faults are either locked and accumulate strain elastically, which is then released instantly in an earthquake, or that they behave more plastically by accommodating constant (or transient) slow slip. They may also accommodate a mixture of both. If lithospheric strain is released in large earthquakes, stress-release continues during the post-seismic period. The postseismic phase includes (a) afterslip on the ruptured fault (e.g., Marone et al., 1991; Perfettini et al., 2010), (b) poro-elastic rebound due to pore fluid pressure changes (e.g., Jónsson et al., 2003; Peltzer et al., 1998) and (c) viscoelastic mantle relaxation (e.g., Nur & Mavko, 1974; Wang et al., 2012). These processes can last months to decades depending on earthquake magnitude and rheological properties, with relocking taking place simultaneously (Bürgmann & Dresen, 2008). Eventually, the seismic cycle returns to the interseismic stage, where strain is being accumulated in a quasi-linear fashion.

Unlike oceanic subduction zones with a well-defined plate interface, the geometry of intercontinental faults is often unknown and slip rates are significantly slower thus leading to an underestimation of the regional seismic hazard potential. In the plate interior, the lithosphere is fractured in a most complex way, probably pre-stressed and can be triggered by small transient stress perturbations (Calais et al., 2016). Consequently,
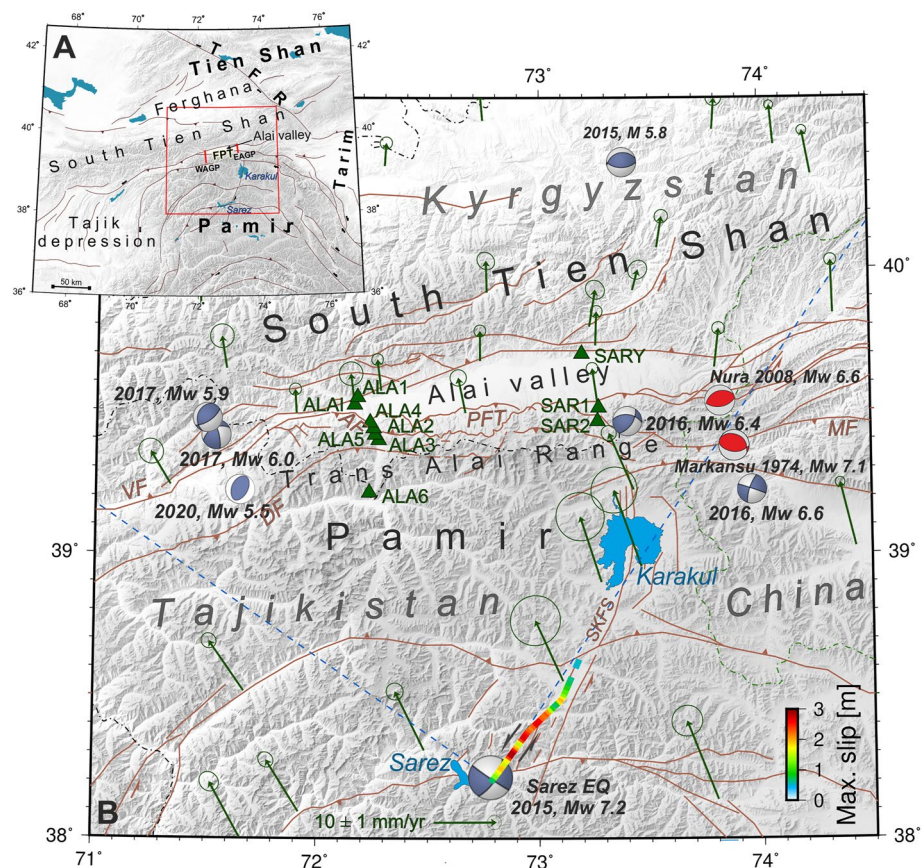
**Figure 1.** (a) Tectonic map of the Alai valley and its enclosing mountain ranges, the South Tien Shan and the north-advancing Pamir, at the northwestern tip of the India-Asia collisional belt. (b) The western and eastern Alai GPS profiles (green triangles) are located in a tensional quadrant of the sinistral 2015 $M_w$7.2 Sarez earthquake (dashed blue lines, focal mechanism from USGS, color-coded co-seismic slip of Metzger et al., 2017). Violet focal mechanisms represent all $M_w \geq 5.5$ earthquakes (GEOFON, 2006), labeled by year and magnitude, that occurred during GPS data acquisition; red mechanisms relate to earthquakes mentioned in the text. Green arrows indicate interseismic GPS rates (Zubovich et al., 2010, 2016). Mapped faults (in brown) from Mohadjer et al. (2016); AF—Aramkungey fault, DF—Darvaz fault, MF—Markansu fault, PFT—Pamir frontal thrust, SKFS—Sarez-Karakul fault system, VF—Vakhsh fault.

continental earthquakes are often unexpected and most fatal, as they often also initiate secondary effects, like landslides or flooding due to blocked rivers. Continental collision zones often behave more like intercontinental than plate-boundary faults; large earthquakes can create highly complex fracture patterns due to dynamics and/or static stress changes (Xu et al., 2020).

The Pamir and the Tien Shan in Central Asia belong to the tectonically most active regions of the India-Eurasian collision zone and are known to host devastating earthquakes (Figure 1a). Examples in the northern Tien Shan are the 1,911 moment magnitude $M_w$8.0 Kebin earthquake (Kulikova & Krüger, 2015) and the 1946 Chatkal earthquake with a body wave magnitude of $M_B$7.5 (Kulikova, 2016), and in the South Tien Shan the 1949 $M_w$7.6 Khait earthquake (Evans et al., 2009; Kulikova, 2016). The 1911 $M_B$7.3 (Kulikova et al., 2016) and 2015 $M_w$7.2 Sarez earthquakes (Metzger et al., 2017; Sangha et al., 2017) ruptured the center of the Pamir and the 1974 $M_w$7.1 Markansu earthquake its northwestern rim (ISC-GEM catalog, Di Giacomo et al., 2015).

A prerequisite for seismic hazard assessment are accurate fault-slip estimates and space-based positioning data (e.g., Global Positioning System [GPS]) are most helpful to constrain them with mm-accuracy. The data is either collected episodically or continuously, and there is a trade-off between spatio-temporal data density and measurement cost: many regional GPS networks comprise either a low station density (~100 km) or rare measurements (~once a year). To improve our understanding of fault slip behavior over the full seismic cycle and detect complex

rupture patterns in this tectonically active region in Central Asia we need high-resolution data both in space and time.

We present new GPS data acquired in continuous- (cGPS) and survey-mode (sGPS) from the Alai valley in southwestern Kyrgyzstan that separates the Pamir in the South and the Tien Shan in the North (Figure 1b). Two ~N-S oriented GPS profiles cross both the Alai valley and the Pamir thrust system representing the active front of the north-advancing Pamir orogen with dense instrumentation. The 4–6 years long GPS time-series provide inter-, co- and postseismic rate estimates in the context of the 2015 $M_w$7.2 Sarez earthquake. This event ruptured the Sarez-Karakul fault system (Figure 1b), a sinistral, NE-trending fault not directly connected to the Pamir thrust system. Our observations provide new insights on the kinematic response of a fault activated by a nearby large earthquake. After a brief introduction to the tectonic setting and the instrumental setup we present the coseismic offsets and post-seismic rate changes caused by the event, compare them to interseismic East rates obtained by satellite radar interferometric (InSAR) time-series and discuss the implications for the faults at the Pamir front.

## 2. Tectonic Setting

The E-W trending Alai valley is a 150 km long, asymmetric intermountain depression of up to 25 km width that is embedded between the two largest orogenic belts of Eurasia: the Tien Shan in the North and the Pamir in the South (Figure 1). While the Tien Shan is an intraplate orogen, the Pamir belongs to the Alpine-Himalayan belt that was formed as a result of the closure of the Tethys paleo-ocean (van Hinsbergen et al., 2012). During the late Oligocene/early Miocene (~25–20 Ma) the former Tarim-Tajik basin was separated by the Pamir. In mid-Miocene (~16–12 Ma) N-S-shortening localized along the Pamir thrust system, consequently forming the Trans Alai range, followed by basin annihilation as already observed West and East of the Alai valley (Coutand et al., 2002). The Cenozoic infill of the Alai valley exhibits a southward increase in thickness from 3.5 to 5.5 km (Coutand et al., 2002.).

The south-dipping Pamir thrust system delimits the Pamir to the North and comprises the Main Pamir thrust, located within the Trans Alai Range (e.g., Gubin, 1940; Nikonov, 1988), and the Pamir frontal thrust (PFT) that separates the Alai valley from the Trans Alai range with a clear morphological expression (e.g., Arrowsmith & Strecker, 1999; Strecker et al., 1995; Sobel & Dumitru, 1997) (Figure 1). The PFT in our study region was formed ~0.7 Ma ago and has remained active since then (Coutand et al., 2002; Strecker et al., 2003). It is divided in three segments that are separated by two transfer zones (Figure 2), all exhibiting kinematic variations of absorbing plate convergence (Arrowsmith & Strecker, 1999). The eastern segment witnesses no Quaternary tectonic activity; fan surfaces are smooth and intact (Arrowsmith & Strecker, 1999; Strecker et al., 2003). Quaternary deformation and background seismicity is offset further South to the E-trending Markansu fault (Schurr et al., 2014). The eastern transfer zone shows evidence for major Quaternary deformation but significant displacement is scarcely found (Arrowsmith & Strecker, 1999). The central segment contains thrust faults, covered in some places by late-Holocene landslides (Arrowsmith & Strecker, 1999). Movement along the fault with a southward dip of 30°–45° is mainly dip-slip with a Holocene slip rate of up to 6 mm/yr (Strecker et al., 2003). The western transfer zone is tectonically the most complex of all segments and consists of en-echelon faults (Arrowsmith & Strecker, 1999). NW-striking, dextral strike-slip faults alternate with SW-trending thrust faults. The westernmost dextral Aramkungey fault (Figures 1b, 3a, and 3b) (Nikonov, 1988) exhibits a dip-slip along-strike across the Altyndara valley (see next paragraph) and accommodates an interseismic slip rate of at least $6.0 \pm 0.8$ mm/yr (Zubovich et al., 2016) and a Holocene slip rate of 2.5–6 mm/yr (Arrowsmith & Strecker, 1999). At the western segment of the PFT, the Alai valley narrows to 3 km before the Pamir and Tien Shan unite orographically. Holocene displacements emphasize thrusting, but the fault surface trace is often buried by landslide sediments (Strecker et al., 2003).

Although the surface trace of the NW-SE-striking Aramkungey fault is not continuously evident, it very probably connects two thrust faults striking WSW-ENE to E-W (Figure 3): A western one emplacing Lower Cretaceous strata on Pliocene to Quaternary and an eastern one emplacing Lower Cretaceous on Upper Cretaceous strata. While the western thrust dips south and has a little deformed succession of the Alai valley foreland in its footwall, the eastern thrust has a more internal (southern) position and dips north, functioning as a "passive" backthrust that borders the large Pik Sverdlova (Figure 3b) triangle zone (Voigt et al., 2020). From west to east, the Aramkungey fault thus mediates a southward step of proven active deformation by about 7.5 km and a change in the
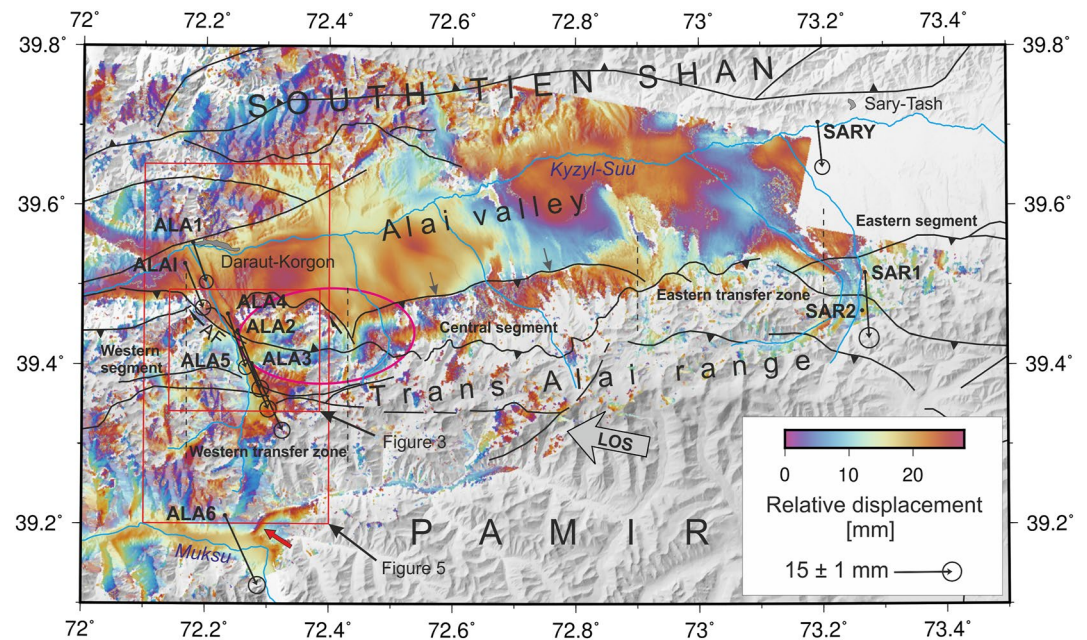
**Figure 2.** Coseismic displacement from the 2015 $M_w$7.2 Sarez earthquake observed by cGPS (black arrows with two-sigma-confidence ellipses) and interseismic satellite radar interferometric. Wrapped interferometric co-seismic fringes in descending view mode (LOS), pointing away from the satellite (Metzger et al., 2017). Gray and red arrows mark sharp interferometric offsets, the pink ellipse highlights deformation fringes, vertical dashed lines separate the Pamir frontal thrust segments, the red rectangles mark the extent of Figures 3 and 5.

thrusting direction from North to South (Figure 3b). No strata older than Lower Cretaceous are exposed anywhere North of the thrust fault labeled "TJ" in Figure 3a. This indicates a thin-skinned structural style where all thrust faults branch from a gently south-dipping basal décollement near the base of the Lower Cretaceous succession. As the Aramkungey fault separates two parts of the thrust wedge sliding on the décollement, it should itself also terminate on this low-angle thrust plane (Figure 3b) at a maximum depth of 2–3 km below the surface.

Both West and East of the Aramkungey fault (Komansu fault scarp, Arrowsmith & Strecker, 1999), the active deformation front is located further north. However, deformed and uplifted strata North of the Aramkungey fault must also be underlain by a décollement fault. Whether this fault (approximate trace dashed in Figure 3a) is presently active together with the Aramkungey fault or the deformation front has stepped back onto the Aramkungey fault from a more external position is unknown.

A detailed seismotectonic analysis of Schurr et al. (2014) revealed a predominant dextral slip along E(SE) trending planes of the PFT, arranged in sub-vertical clusters underneath a décollement layer. Trenching data provide evidence of at least two full ruptures of the central PFT segment within the last 5,000 years and a few partial ruptures at the western end of the segment (Patyniak et al., 2021). In instrumental times the 1974 $M_w$7.1 Markansu earthquake and the 2008 $M_w$6.6 Nura earthquake (Figure 1) ruptured thrust faults East of the eastern PFT segment (Sippl et al., 2014) (Figure 1b). Slip might also occur on faults below the sedimentary layer further North, or historic surface expressions might have been eroded (Patyniak et al., 2021).

GPS data suggest that the eastern Trans Alai range accommodates more than a third (10–15 mm/yr) of the India-Asian convergence and 5–6 mm/yr dextral shear. The western Trans Alai Range accommodates a similar amount of shortening (12–13 mm/yr) but increased dextral shear (8–9 mm/yr) (Zubovich et al., 2010). At least $7.0 \pm 0.8$ mm/yr shortening and $7.0 \pm 0.8$ mm/yr shear are accommodated at the PFT (Zubovich et al., 2016) with the largest portion of slip being attributed to the dextral Aramkungey fault between the two stations ALA3 and ALA2 in 5 km distance ($3.8 \pm 0.8$ mm/yr, respectively, $4.7 \pm 0.8$ mm/yr) (Figure 1). These rates are in agreement with the kinematics derived from structural and stratigraphic field data (e.g., Coutand et al., 2002) and the gravitational, westward mass outflux of the West Pamir into the lower Tajik depression (Ischuk et al., 2013; Metzger et al., 2020; Schurr et al., 2014; Zubovich et al., 2016). Highest slip rates are observed on the Vakhsh and Darvaz
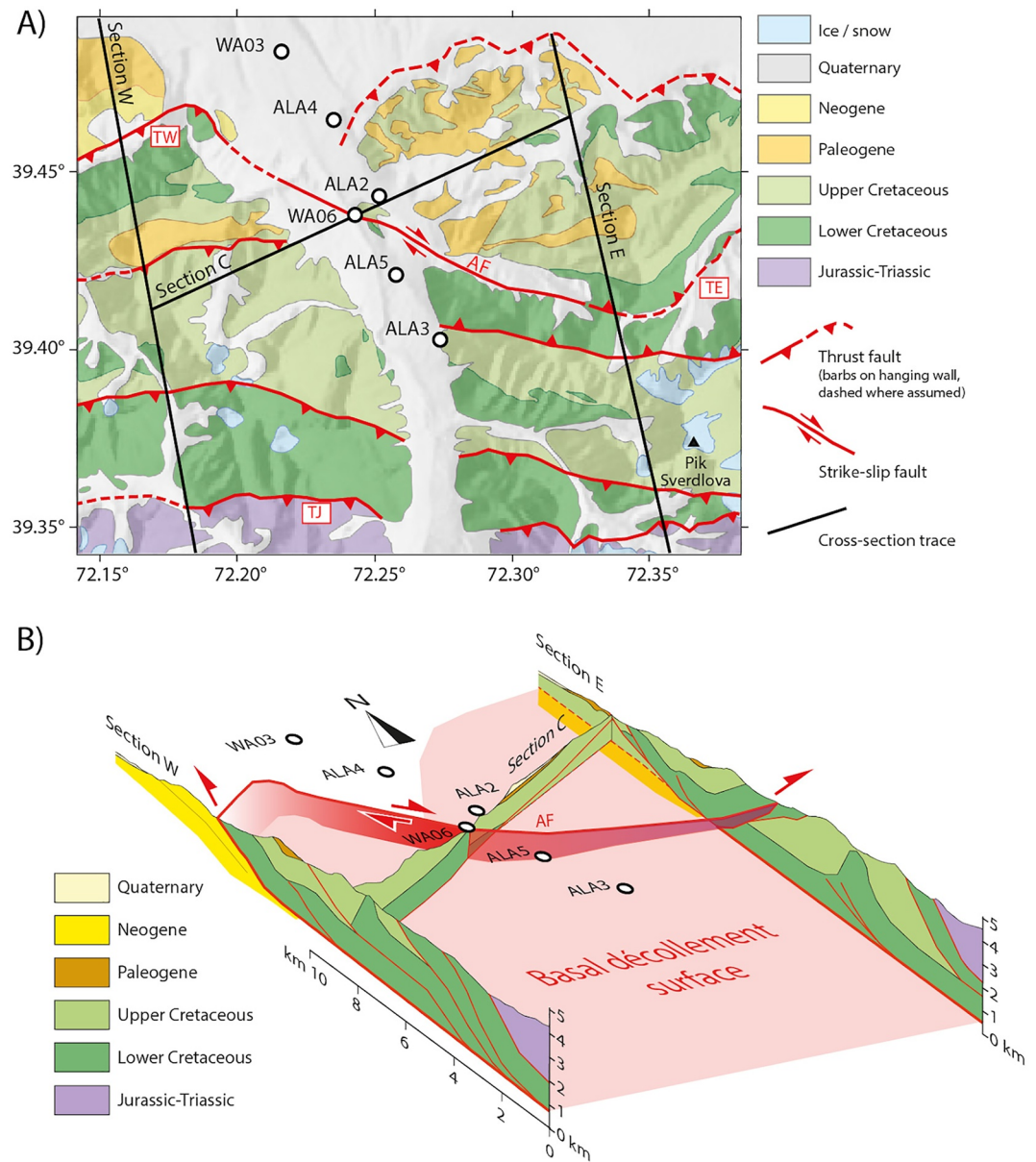
**Figure 3.** (a) Simplified geological map of the frontal Pamir thrust belt around the Aramkungey fault, based on 1:50,000 maps (Zaalaian Exploration Team, 1993) and own observations (see Figure 2 for spatial extent). Only major faults are shown. The Aramkungey fault (AF) connects a north-vergent thrust fault in the West (TW) with a south-vergent backthrust in the East (TE). (b) Two transverse cross-sections "W" and "E" and central section "C" crossing the Aramkungey fault, shown as a fence diagram. Section locations in Figure 3a. The Aramkungey fault is expected to terminate on the basal décollement surface of the thrust belt.

faults (Figure 1) forking from the PFT at the western end of the Alai valley toward WSW and SW, respectively, squeezing out the intervening triangular block to the southwest. The dextral-transpressive Vakhsh thrust accommodates 22 + 5/-4 mm/yr of slip, and the sinistral-transpressive Darvaz fault accommodates ~18 mm/yr of slip (Metzger et al., 2020; Mohadjer et al., 2010). The East Pamir, in contrast, moves northwards nearly en-bloc and we do not observe an eastward escape toward the Tarim basin (Avouac et al., 1993; Reigber et al., 2001). The NE-trending, sinistral Sarez-Karakul fault system in the central Pamir presumably accommodates this kinematic difference of East and West Pamir by 3–4 mm/yr of sinistral slip (Metzger et al., 2017).

During our GPS data collection, the region was struck by several M6+ earthquakes, of which three are relevant to our analysis: the 7 December 2015, $M_w$7.2 Sarez, Central Pamir, earthquake ruptured an 80 km-long segment of

the Sarez-Karakul fault system with as much as ∼3 m of sinistral slip (Figure 1) (Metzger et al., 2017). High-rate GPS stations GPS stations in NE-Afghanistan (250 km from the epicenter) and the western Alai valley (Metzger et al., 2017) observed cm-displacement and survey GPS dy GPS data in the West Pamir also support the assumption of co-seismic activation (Metzger et al., 2020). Six, respectively 12 months later, the $M_w$6.4 Sary-Tash thrust event (Funning & Garcia, 2019; Vajedian et al., 2017) and the $M_w$6.6 Aketao (Muji) dextral-slip earthquake (e.g., Wang et al., 2017; Feng et al., 2017) ruptured the Pamir's northern rim. It is debated, if they form a sequence or not (Bloch et al., 2021; Jin et al., 2022; Li et al., 2019).

## 3. The Alai GPS Network and Data Processing

To better understand the kinematic behavior of the PFT in 2013 we installed four continuously-operated GPS stations along a N-S oriented profile in the western Alai valley (WAGP, Figure 1) (Zubovich et al., 2016). In 2014 this profile was densified and elongated by six sGPS markers and in 2015 by another three cGPS stations. The WAGP stretches over 40 km from the southernmost Tien Shan across the Alai valley and the Trans Alai range and thus covers the surface expressions of the full Pamir thrust system, with the smallest inter-station distance (∼2.5 km) across the Aramkungey fault. A second N-S profile with three cGPS stations was installed in the eastern Alai valley (EAGP). It has a total length of 27 km and crosses the PFT.

The WAGP was designed such that we can quantify the relative convergence between the South Tien Shan and the North Pamir with a particular focus on the slip mechanism on the PFT fault strand as well as eventual shortening within the Trans Alai Range and the sediments of the Alai valley. If compared to data from the WAGP, the sparse EAGP allows to identify slip variations along the PFT.

The limiting factor of the network design was the terrain that impedes (direct) visibility between the stations to enable data transfer, and solar power supply, particularly during winter time. Primary, independent stations (ALAI/ALA6/SARY) that collect data from secondary stations via wireless ethernet transmission are built as Remotely-Operated Multi-Parameter Stations (Figure S1 in Supporting Information S1) (Schöne et al., 2013; Zech et al., 2021). All stations are operating autonomously and automatically and maintenance is limited to summer and autumn. They are equipped with Septentrio AsteRx2e GPS receivers and NavXperience antennas. Three stations (ALAI, ALA2 and ALA4) are installed in alluvial conglomerates. To improve their stabilization, the metal antenna mounts were cemented into a buried cube of 70 cm length. The antenna mounts of all other stations were anchored to bedrock. More information on the instrument setup and communication can be found in the supplementary material. The stations sample at 1 Hz and transmit the raw data automatically to our data storage facilities during daytime. Data loss occurred mostly in the first year (see the full time-series in Figures S3a and S3b in Supporting Information S1).

The sGPS markers were measured annually from 2014 to 2019 in the time period between July and September (Metzger, Kakar, et al., 2021). All but two markers were installed by drilling and glueing a 10 cm-long stainless-steel bolt of 1 cm diameter into bedrock. Two markers (WA02 and WA03) were installed in alluvial conglomerates; they consist of a 1.5 m-long and 2 cm-wide steel rod, hammered and cemented into the ground (Figures S2a and S2b in Supporting Information S1). Each point was measured at minimum for 48 hr using Topcon PG-A1 antennas fixed on a vertical rod 15 cm above ground (Figures S2c and S2d in Supporting Information S1). The rod was centered in a triangular instrument table that was horizontally adjusted by three extendable screws. The quasi-four-legged setup was a challenge to stabilize and might have caused repeatability noise. The data was sampled at 30 s using Topcon GB-1000 receivers; power supply was ensured by car batteries and solar panels.

We processed the data with the GAMIT software using standard parameters (Herring et al., 2009, 2018) to obtain daily positions (Figure S3 in Supporting Information S1). We included data from all CAIAG/GFZ and IGS regional GPS stations (in the area from 66° to 80° in longitude and from 34° to 45° in latitude) as well as the Eurasian reference stations of the IGS network (43 in total) (Johnston et al., 2017) available at https://cddis.nasa.gov and http://garner.ucsd.edu. The time series were derived by combining the daily GAMIT solutions with the GLOBK software (Herring et al., 2009, 2015).

**Table 1**
*cGPS Locations, Epicentral Distances and Co-Seismic cGPS Displacements Caused by the 2015 $M_w$7.2 Sarez Earthquake*

| | Coordinates | | | Displacement (mm) | | | |
|---|---|---|---|---|---|---|---|
| Station | Lon. (°) | Lat. (°) | Epicent. distance (km) | East | North | Up | Horizontal |
| SARY | 73.19371 | 39.70529 | 169.7 | 1.3 ± 0.6 | −11.8 ± 0.9 | 3.0 ± 5.8 | 12.4 |
| SAR1 | 73.26953 | 39.51603 | 151.0 | 1.0 ± 0.9 | −16.9 ± 0.9 | 3.4 ± 6.1 | 17.2 |
| SAR2 | 73.26478 | 39.46850 | 145.8 | | | | |
| ALA1 | 72.17914 | 39.55298 | 157.8 | 3.6 ± 0.7 | −10.1 ± 0.8 | 2.6 ± 9.5 | 11.9 |
| ALAI | 72.16589 | 39.52653 | 155.4 | 4.8 ± 0.6 | −11.0 ± 0.9 | 3.1 ± 5.8 | 12.7 |
| ALA4 | 72.23589 | 39.46355 | 146.8 | 5.5 ± 0.6 | −14.4 ± 0.8 | −3.6 ± 2.0 | 15.4 |
| ALA2 | 72.25173 | 39.44326 | 144.2 | 6.1 ± 0.7 | −15.2 ± 0.8 | 2.8 ± 7.8 | 15.9 |
| ALA5 | 72.25779 | 39.42136 | 141.7 | 6.9 ± 0.6 | −15.8 ± 0.9 | 3.7 ± 5.3 | 17.0 |
| ALA3 | 72.27453 | 39.40224 | 139.2 | 7.8 ± 0.6 | −17.2 ± 0.9 | 2.4 ± 4.0 | 19.4 |
| ALA6 | 72.23272 | 39.21072 | 120.7 | 8.0 ± 0.7 | −18.0 ± 0.9 | 3.5 ± 6.7 | 19.7 |

*Note.* Station SAR2 was out of service during the event.

## 4. The Seismic Cycle, Observed by GPS and InSAR

The 2015 $M_w$7.2 Sarez and the 2016 $M_w$6.4 Sary-Tash earthquakes (Figure 1) caused significant seismic offsets in our GPS time-series (see time-series in Figures S3 and S4 in Supporting Information S1), providing insight into the full seismic cycle of a fault activated by a nearby large earthquake. We analyzed the co- and postseismic GPS rates and compared them to interseismic rates constrained before the Sarez earthquake, and rates derived from satellite interferometric radar (InSAR) time-series starting at least 8 months after the Sarez earthquake.

### 4.1. Coseismic Offsets

The cGPS time-series show that the 2015 $M_w$7.2 Sarez earthquake caused static offsets at all stations in the Alai valley, located at 120–170 km distance from the epicenter. The observed offsets are on cm-level or less, hence, it is crucial to properly estimate the offset overlaid by secular fault loading. We therefore first calculated baselines between our network stations and other regional stations unaffected by the earthquake (Wdowinski et al., 1997) to reduce the systematic noise (Figure S5 in Supporting Information S1). We then built linear regressions of data acquired 60 days before and 60 days after the earthquake to determine the coseismic offset. This time window represents a good trade-off to limit daily scatter but suppress the influence of seasonal effects. Daily solutions with large deviations or uncertainties were excluded from the regression. For each station of the Alai network we created 25 baselines, extracted the individual, and calculated the mean offset for each component while excluding anomalous results (Table 1, exemplary baseline plots are shown in Figure S5 of the Supporting Information S1). The corresponding uncertainties were derived by the standard deviation of the individual offsets.

We found that the EAGP stations moved 12–17 mm southwards during the Sarez earthquake; the WAGP stations moved 3–8 mm eastward and 10–18 mm southward (Figure 2 and Table 1). The stations closest to the epicenter observed the largest co-seismic offsets. Largely within the respective uncertainty ranges (5–12 mm), all stations were coseismically uplifted by 2.4–3.7 mm, except for station ALA4 that exhibits subsidence of −3.6 ± 2.0 mm. The offsets are also presented along profiles that cross the Pamir front perpendicular to the Pamir front strike (Figure 4).

In the same fashion we searched for potential offsets caused by the other nearby $M_w$5.5+ events (Table S1 in Supporting Information S1) and identified the 2016 $M_w$6.4 Sary-Tash earthquake as a second event, detected by station SARY on the EAGP profile only, where we measured a southward offset of 8.1 ± 1.2 mm and an eastward offset of 4.8 ± 1.3 mm. The other two EAGP stations were not operating at that time. We conclude that in the western Alai valley the co-seismic response to the Sary-Tash earthquake is below the cGPS detection threshold.

We also estimated the co-seismic offsets using a trajectory model that accounts for a linear trend, (semi-)annual oscillation and offsets (Figures S3a and S3b in Supporting Information S1) (Metzger et al., 2013). This independent
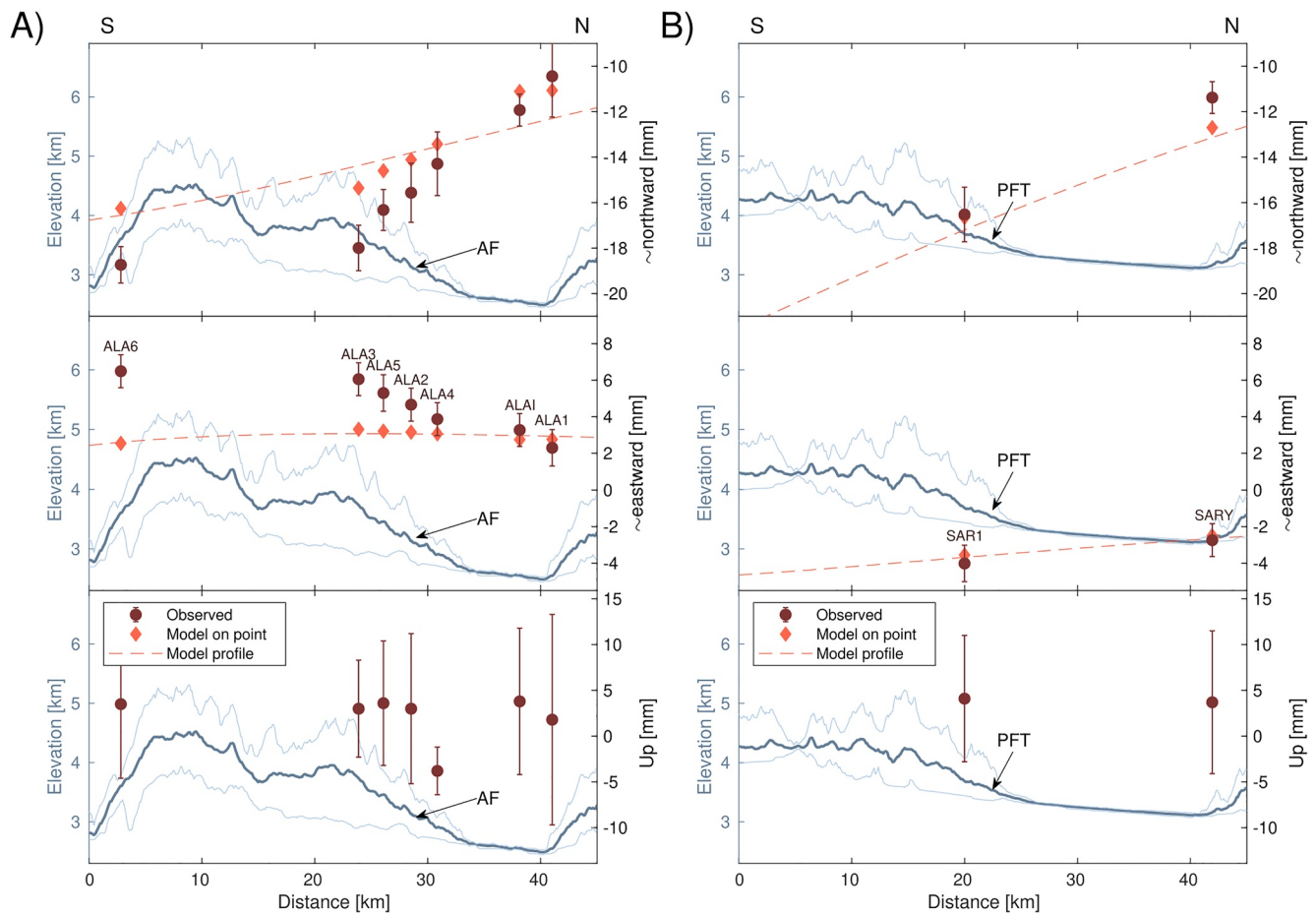
**Figure 4.** Co-seismic cGPS offsets (dark red circles) along (a) the WAGP and (b) the eastern Alai valley, in comparison to horizontal model predictions on-site (diamonds) and along a straight N-S profile (dashed line) (Metzger et al., 2017). The offsets are rotated by 5°, resp. 15° counterclockwise and correspond to ~northward (or PFT-perpendicular), ~eastward (or PFT-parallel) and vertical offsets. Minimum, median and maximum elevation of a 10 km wide swath is indicated in blue. AF: Aramkungey fault, PFT: Pamir frontal thrust.

approach resulted in a consistently higher eastward offset of 1–3 mm and lower southward offset of ∼2 mm (Figure S6 in Supporting Information S1). This systematic bias is caused by the (unmodeled) visco-elastic relaxation component that affects the data only in the 1–2 months following the earthquake with amplitudes just at the detection threshold (Figures S3c and S3d in Supporting Information S1). But—as we show later—both methods do reproduce the local, residual deformation pattern. In the following, we only show the offsets derived from the baseline estimates.

### 4.2. Post-Seismic Rates Following the 2015 Sarez Earthquake

To better understand the crustal response to the 7 December 2015 $M_w$7.2 Sarez earthquake we analyzed two postseismic phases of the cGPS time-series, starting from July 2016, respectively, 2018 and lasting two years each. We excluded data collected in the first 7 months after the event, because they either were contaminated by postseismic relaxation during the first 1–2 months following the earthquake (Figures S3c and S3d in Supporting Information S1), the 26 June 2016 $M_w$6.6 Sary-Tash earthquake (Table 1, Figure S2 in Supporting Information S1) and/or the stations were temporarily out of service.

We used the GLOBK software (Herring et al., 2009, 2015) to uniformly constrain the apriori daily positions derived from GAMIT (Herring et al., 2018) and selected a subset of stable stations using the *glorg* program. We then estimated the rates and their uncertainties from our time-series of the cGPS observations, while excluding outliers and removing seasonal variations. The resulting rate uncertainties were normalized by their length of
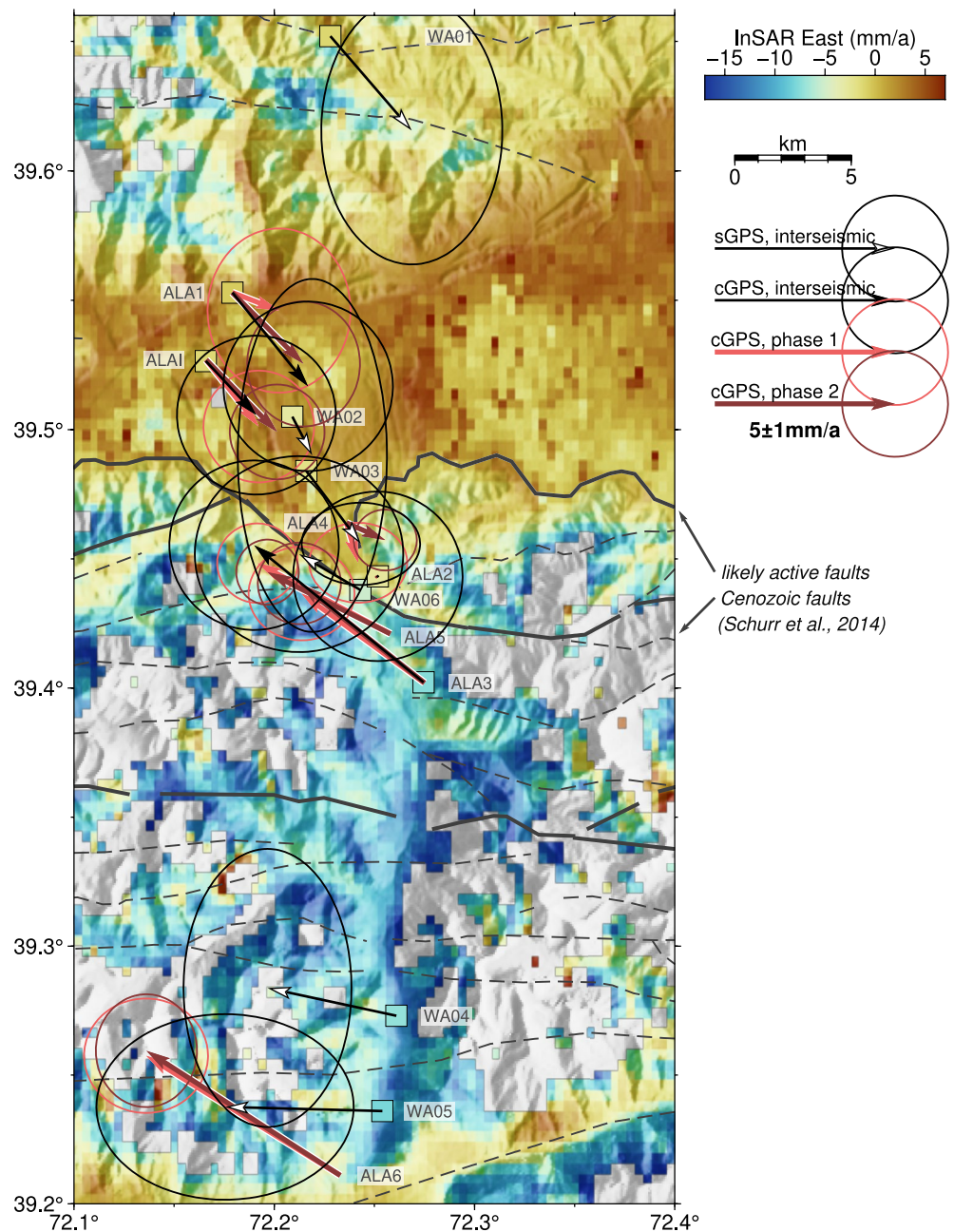
**Figure 5.** Interseismic sGPS and inter- (Zubovich et al., 2016) and post-seismic cGPS rates of phase 1 and 2 of the western Alai valley, all relative to station ALA2. Background map and color-coded squares are interseismic GPS, respectively interseismic satellite radar interferometric East rates relative to stable Eurasia (Metzger, Lazecky, & Maghsoudi, 2021).

2 years (Geirsson et al., 2006). The rates are presented in map view (Figure 5) and in profile view (Figure 6), both relative to ALA2 (Table 2)—the central station in the profile and closest to the fault trace—to highlight the detailed kinematics at the Aramkungey fault segment.

### 4.3. Complementary Rates From Survey GPS and InSAR Time-Series

Interseismic rates of the WAGP prior to the Sarez earthquake have already been published (Zubovich et al., 2016); we complement them with linear sGPS rates (Metzger, Kakar, et al., 2021) and high-resolution East rates obtained from InSAR time-series analysis (Metzger, Gągała, et al., 2021; Metzger, Lazecky, & Maghsoudi, 2021).
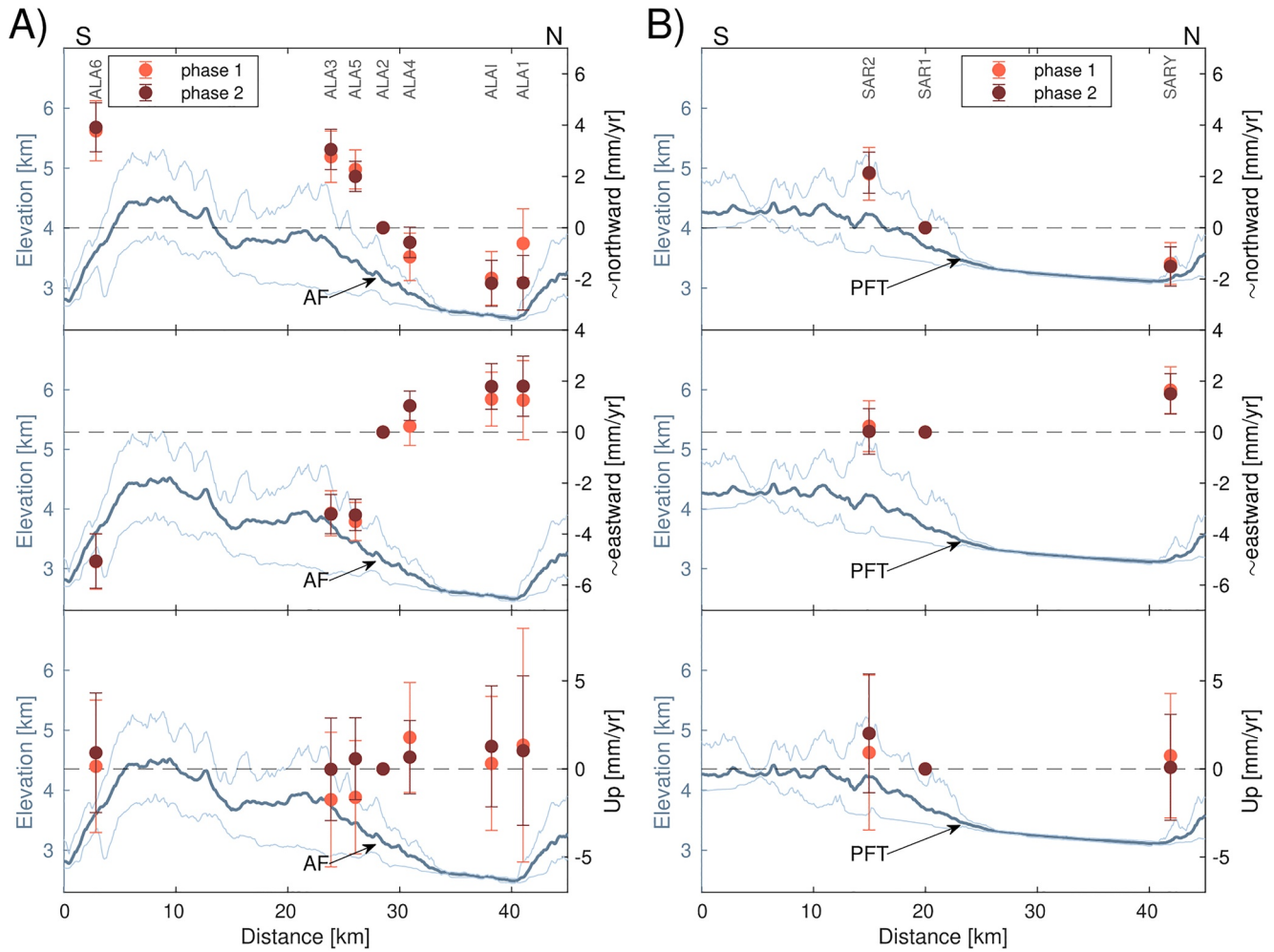
**Figure 6.** Post-seismic cGPS rates during phase 1 (month 8–31) and phase 2 (month 32–55) along the (a) WAGP and (b) EAGP, in comparison to minimum, median and maximum height of a 10 km wide topographic swath (in blue). Rates are relative to station (a) ALA2 and (b) SAR1, rotated counterclockwise by (a) 5°, respectively (b) 15° and thus correspond to PFT-perpendicular (∼northward), PFT-parallel (∼eastward), and vertical rates. AF: Aramkungey fault, PFT: Pamir frontal thrust.

**Table 2**
*Postseismic cGPS Rates Relative to the Station SAR1 (EAGP) and ALA2 (WAGP) for Months 8–31 (Phase 1) and 32–55 (Phase 2) After the 2015 $M_w$7.2 Sarez Earthquake*

| Station | Distance (km) | North (mm/yr) | | East (mm/yr) | | Up (mm/yr) | |
|---|---|---|---|---|---|---|---|
| | | Phase 1 | Phase 2 | Phase 1 | Phase 2 | Phase 1 | Phase 2 |
| SARY | −21.1 | −0.9 ± 0.9 | −1.1 ± 0.8 | 2.0 ± 0.8 | 1.8 ± 0.8 | 0.8 ± 3.5 | 0.1 ± 3.0 |
| SAR1 | 0.0 | – | – | – | – | – | – |
| SAR2 | 5.3 | 2.1 ± 1.0 | 2.1 ± 0.9 | −0.3 ± 1.0 | −0.5 ± 0.8 | 0.9 ± 4.4 | 2.0 ± 3.4 |
| ALA1 | −12.2 | −0.5 ± 1.6 | −2.0 ± 1.2 | 1.3 ± 1.4 | 2.0 ± 1.1 | 1.4 ± 6.6 | 1.0 ± 4.2 |
| ALAI | −9.3 | −1.9 ± 1.1 | −2.0 ± 0.9 | 1.5 ± 1.0 | 2.0 ± 0.9 | 0.3 ± 3.8 | 1.3 ± 3.4 |
| ALA4 | −2.3 | −1.1 ± 0.8 | 0.5 ± 0.6 | 0.3 ± 0.9 | 1.1 ± 0.6 | 1.8 ± 3.1 | 0.7 ± 2.1 |
| ALA2 | 0.0 | – | – | – | – | – | – |
| ALA5 | 2.4 | 2.0 ± 0.8 | 1.7 ± 0.6 | −3.7 ± 0.8 | −3.4 ± 0.6 | −1.6 ± 3.2 | 0.6 ± 2.3 |
| ALA3 | 4.6 | 2.5 ± 0.9 | 2.8 ± 0.8 | −3.4 ± 1.0 | −3.5 ± 0.8 | −1.7 ± 3.8 | 0.0 ± 2.9 |
| ALA6 | 25.9 | 3.3 ± 1.1 | 3.5 ± 1.1 | −5.4 ± 1.2 | −5.4 ± 1.0 | 0.2 ± 3.8 | 0.9 ± 3.4 |

The sGPS positions resulting from the combined GAMIT processing were visually checked for outliers. Linear rates and corresponding uncertainties were extracted using a weighted linear regression and averaged standard deviations. All sGPS positioning data collected after the 2015 $M_w$7.2 Sarez earthquake were corrected for the expected co-seismic offset using interpolated cGPS offset data (Table 1 and Figure S4 in Supporting Information S1). The standard deviations are rather large due to significant data scattering, probably caused by the rickety instrument setup (Figure S2c in Supporting Information S1), and consider these rates as inferior.

The InSAR East rates are derived from C-band (i.e., 5.6 cm wavelength) radar data of the European Copernicus Sentinel-1 radar mission (Metzger, Gągała, et al., 2021; Metzger, Lazecky, & Maghsoudi, 2021). Imagery was acquired in ascending (orbit number 100) and descending (005) view mode, starting from eight, respectively 16 months after the Sarez earthquake, both ending in June 2020. The differential interferograms usually cover 12–48 days and were automatically generated, multi-looked (downsampled) to ∼100 m, filtered using an adaptive-phase filter and unwrapped to provide relative displacement data in two look directions of the satellite (Lazeckỳ et al., 2020). After an additional multilooking to ∼400 m the interferograms served as database for a small-baseline time-series analysis (Morishita et al., 2020) that automatically accounts for atmospheric signal contributions (Yu et al., 2018), suppresses interferometric noise, identifies outliers using a variety of quality markers and estimates rates using a linear fit to the time-series. The final rates were Gaussian-filtered in space (2 km) and time (∼2 months) (Hooper et al., 2007). We used interpolated GPS rates (Zubovich et al., 2010) to fix the North component, extract the East rate component and tie the rates to a Eurasian stable reference frame (Figure 6) (Ou, 2020). Rate uncertainties are ∼1.5 mm/yr. More details on the processing and results can be found in Metzger, Gągała, et al. (2021).

## 5. Discussion

Our analysis and interpretation of along-strike slip behavior of the Pamir frontal thrust and the dextral-transpressive Aramkungey segment in particular lean on different data types with different sampling rates covering various time spans of the seismic cycle embracing the 2015 $M_w$7.2 Sarez earthquake. Co-, post- and interseismic signals are at mm- to cm-scale and thus close to the noise level; isolating the tectonic signal from unwanted instrumental, atmospheric, seasonal or near-surface effects is most crucial and the data treatment differs for each data type or sampling rate. We only consider observations to be significant for interpretation if they are supported either by adjacent stations or independent data covering the same period. We rank the cGPS observations as being most reliable, followed by InSAR rates and, finally, the interseismic sGPS rates.

### 5.1. Static Displacements

The static, co-seismic cGPS displacements (Figure 3) image the detailed response of the Earth's crust to the Sarez earthquake in 120–170 km distance. All stations are located in the same tensional quadrant of the rupture mechanism (Figure 1b) and were pulled toward the earthquake epicenter and its NE-striking rupture plane (Metzger et al., 2017), that is the WAGP stations toward SSE, the EAGP stations toward South. The epicentral drag of all stations is similar and stations closest to the epicenter exhibit the highest offset. Amplitudes agree to the first order with co-seismic offset predictions based on a homogeneous half-space model (Metzger et al., 2017).

When the offsets are displayed along profiles crossing the Pamir front and decomposed into a front-parallel and -perpendicular component, the offsets decay distinctly across the front (Figure 4). This is obvious in particular at the dense, western profile: while the southernmost two stations (ALA6, ALA3) are offset almost equally, we observe a significant offset decrease at the stations further North. The co-seismic slip model of Metzger et al. (2017) assumes a homogeneous substrate, slightly underpredicts the ∼southward offset by ∼3 mm and fails to represent the ∼eastward offset by up to ∼4 mm of the cGPS stations near or South of the Aramkungey fault. It also does not foresee such a rapid offset decrease. This is significant since the EAGP predictions and observations fit much better. Our observations could be explained with a co-seismic, sinistral (retrograde) reorganization of the heavily fractured fault zone, which could only be satisfyingly modeled using a inhomogeneous model setup allowing for slip on local structures, for example, the PFT and/or the Aramkungey fault. Given the sparse amount of cGPS data, the high uncertainties of the sGPS and InSAR offsets and the highly three-dimensional nature of the local fault geometry, we refrain from any rather speculative modeling attempt.

The observation of co-seismic offset across the PFT is also supported by local surface deformation observed by a co-seismic radar interferogram (Metzger et al., 2017) exhibiting a range decrease of ∼1 fringe (corresponding to ∼2.8 cm) on the hanging wall toward the surface trace of the PFT, just East of the Aramkungey fault segment (pink ellipse in the Figure 2). At the central PFT segment we observe sharp offsets of 5–10 mm in line-of-sight, indicating that the hanging wall of the PFT was displaced away from the satellite relative to the footwall over remarkable tens of km (marked by gray arrows in Figure 2). We rule out atmospheric errors as the sharp offsets are also observed on a second, independent interferogram with a different view angle (Metzger et al., 2017). We also rule out a bias caused by a poor digital elevation model as the signal cannot be reproduced in, for example, postseismic interferograms (Bloch et al., 2021).

Most interestingly, the sign of the offset seems to flip along-strike. We can limit the occurrence of these offsets to the time window of 19 days before and 5 days after the Sarez earthquake, which are the acquisition dates of the two radar images forming the interferogram. Thus, the PFT activation observed in the interferogram must have occurred during the earthquake (as constrained by cGPS time-series) and/or in the subsequent 5 days. These signals could be explained by the lowering of the hanging fault wall, relative to the footwall, due to its greater displacement toward the epicenter. Faults in the region are generally assumed to exhibit co- (Teshebaeva et al., 2014) or interseismic (Metzger et al., 2020) slip on low-friction décollements (e.g., Chen et al., 2004; Hamburger et al., 1992; Schurr et al., 2014).

Co-seismic activation of neighboring faults has already been reported using InSAR data (e.g., Fialko et al., 2002; Elliott et al., 2016; Wright et al., 2001). A particularly impressive example is the complex fracture pattern caused by the 2019 $M_w$7.1 Ridgecrest earthquake that induced slip and creep on the conjugate Garlock fault as observed by radar interferograms (Ramos et al., 2020; Xu et al., 2020). Both GPS and InSAR data testimony that the Pamir thrust system was co-seismically activated and exhibits retrograde mm-slip along tens of km. Conjugate slip can be triggered either dynamically by the seismic waves passing by (Velasco et al., 2008), or mechanically, in our case by pulling the upper crust material toward the epicenter inducing slip along neighboring faults with low friction properties.

If we assume that the PFT accommodates at least 9 mm/yr of slip during the interseismic period, our observations indicate that the Sarez earthquake set back the system's stress level equal to ∼1 year of constant loading.

The northernmost stations of the WAGP (ALAI and ALA1) are clearly positioned North of the Pamir frontal thrust, but nevertheless exhibit a slightly different offset. If their difference is significant, this could either be due to co-seismic relaxation of a fault hidden under the alluvial sediments (Coutand et al., 2002), or caused by a relaxation of the latter that are under constant, interseismic N-S-compression.

Except for station ALA4, located at the footwall closest to the Aramkungey fault, all stations of the WAGP exhibit a co-seismic uplift between 2.4 and 3.7 mm, which lies within the respective measurement uncertainties (Figure 4). If this consistency in uplift is to be trusted, it would mean that the whole Northern Pamir Front was slightly uplifted by the earthquake, possibly, due to partial compressional stress release (Figure 2).

## 5.2. Post-Seismic Displacements

Postseismic rate changes across the Pamir front are subtle in map view (Figure 5) and, again, better visualized if the rates are plotted along profiles and decomposed into front-parallel (∼eastward) and front-perpendicular (∼northward) components (Figure 6). As the rates are derived from baselines to a station roughly at the center of the profile and closest to the fault trace,—ALA2 in the WAGP, and SAR1 in the EAGP—all rates are plotted relative to these. The slip sense of the Aramkungey fault flipped from sinistral (during the co-seismic phase) to dextral. Both, front-parallel and -perpendicular WAGP rate changes show a slight, absolute increase from phase 1 to phase 2 to a final 6 mm/yr of ∼N-S-shortening, and 7 mm/yr of dextral shear, suggesting an increase in strain accumulation. Interestingly, dextral shear varies more across the Aramkungey fault than shortening. The two stations closest to the Aramkungey fault on the southern side—ALA3 and ALA5, at only ∼2.5 km distance—exhibit the same front-parallel motion. In phase 1, the stations ALA2 and ALA4, closest to the fault on the northern side, behave similarly to the southern stations, suggesting that the Aramkungey fault is either completely unlocked by the Sarez earthquake and its sides slide freely relative to each other, or the fault locking has only yet affected a corridor up to 2.5 km width.

Jin et al. (2022) used forward and inverse models, a subset of the GPS time-series presented here, and post-seismic InSAR data to quantify the individual spatio-temporal contribution of afterslip, poro-elastic rebound and visco-elastic relaxation following the Sarez earthquake. It appears that the postseismic deformation affected only the near-field (10–100 km), ceased after ~5 years, and was mostly caused by afterslip at the northernmost rupture segment. Visco-elastic contributions were below the geodetic detection threshold, which can be explained with a relatively strong lithosphere containing amalgamated blocks and deep-rooted faults that accommodate most of the internal deformation (Avouac & Tapponnier, 1993; Hubbard & Shaw, 2009). These findings are supported by a GPS trajectory model (Metzger et al., 2013) indicating that an additional viscoelastic relaxation term would improve the data fit during the first ~1–2 months following the Sarez earthquake (Figure S3 in Supporting Information S1), so we may exclude viscoelastic behavior while interpreting the velocities estimated 8+ months later.

Elastic screw dislocation models predict that the steepness of the rate gradient across a locked strike-slip fault relates to the locking depth such that 50% of the rate change across the fault occurs within a corridor sized twice the locking depth (Savage & Burford, 1973). For the Aramkungey fault this would suggest a locking depth of 1–2 km or less, which is approximately half of the distance to the basal décollement.

Sliding can not occur across the fault due to its verticality, so in this direction distributed elastic strain arises in an unconsolidated volume in a strip no less than 7.5 km (distance ALA3-ALA4) wide around the fault, explaining the gentler gradient. During phase 2, the behavior of ALA2 and ALA4 slightly changes, which suggests the expansion of the deformation zone toward North.

The strongest rate variation between the two postseismic phases is observed at the northernmost station of the western profile, ALA1, with a significant front-perpendicular rate increase of 1.5 mm/yr, but no significant change in the front-parallel direction. If significant, this may suggest that one of the thrust faults hidden in the sediments of the Alai valley was active during the first post-seismic phase with a reverse sense of slip.

Both Alai GPS profiles were affected by similarly-sized offsets (Figure 4, Table 1), but the EAGP time-series do not show significant non-linear, post-seismic effects (Figure 6b). This might indicate that the eastern PFT is not affected by the westward escape of the West Pamir, and is kinematically decoupled from the western PFT.

In the vertical rates we observe—within uncertainties—an increased uplift of WAGP stations located in the PFT footwall and an opposite behavior in the EAGP. If this pattern is real, it might represent postseismic alluvial sediment compression in the western Alai valley.

## 5.3. Transition to the Interseismic Stage

Once postseismic rates equal interseismic rates, a fault system has returned to the interseismic stage of the seismic cycle. This is best checked by overlying postseismic and interseismic rates (acquired prior to the Sarez earthquake (Zubovich et al., 2016)) in map view (Figure 5). We complement those with postseismic sGPS rates acquired between 2014 and 2019, and high-resolution InSAR East rates. To highlight the kinematics near the Aramkungey fault and mitigate potential reference frame shifts, we plot the rate vectors relative to station ALA2, the cGPS station located closest to the Aramkungey fault surface trace. cGPS stations ALA4, ALA5 and ALA6 were installed only shortly before the Sarez earthquake and lack interseismic rate estimates. Given the relatively large uncertainties of the interseismic rates we focus on general trends in space and time rather than a quantitative interpretation of each station. The sGPS rates are in general agreement (within uncertainties) with the other data sets, and serve as supporting information.

The stations far North from the Aramkungey fault seem to have returned to the interseismic stage rather quickly, at least in the post-seismic phase 2 (Figure 5). The stations next to the Aramkungey fault (ALA3, maybe ALA4 and ALA5) have probably not yet fully returned to the interseismic stage where we observe a larger rate change across the fault. Rate differences across the fault before and after the earthquake show that the relative rate ALAI-ALA3 temporarily dropped to 78%, and then reached 85% in phase 1 and 2, and the relative rate ALA2-ALA3 temporarily dropped to 70%, respectively 73% of the pre-event rate difference. Thus, near the Aramkungey fault and 4.5 years after the earthquake pre-event strain conditions have not yet been fully recovered.

The InSAR East rates exhibit average surface deformation between 8 months to 4.5 years after the Sarez earthquake (Figure 5). The rates show the westward motion of the Trans Alai range with respect to the Alai valley and the adjacent South Tien Shan. Average rate differences between the Trans Alai and the Alai valley deposits are

~6–8 mm/yr, which is at the lower boundary of observed interseismic fault slip rates of the Pamir frontal thrust (Metzger et al., 2020; Zubovich et al., 2016), agreeing to the postseismic cGPS rates. Further East, at the longitude of the WAGP, dextral slip on the Pamir front has been constrained to be of ~7 mm/yr (Metzger et al., 2020). The InSAR rates show a sharp eastward rate change across the Aramkungey fault, supporting a shallow locking depth of 1–2 km or less. As the input interferograms were strongly filtered (Lazeckỳ et al., 2020) we cannot resolve potential shallow fault creep. East and West of the Aramkungey fault, mapped faults (Schurr et al., 2014) also show significant rate changes, which could indicate that these strands are also active. The InSAR rate map also shows a strong gradient at the southern end of the Trans Alai range and the WAGP. Most probably, these are strong near-surface effects due to slope processes and seasonal water load of the Muksu river valley draining the ~70 km-long Fedchenko glacier, one of the largest glaciers on Earth. It is worth noting, however, that these slopes also seemed to be activated during the Sarez earthquake as observed in the coseismic interferogram (red arrow in Figure 2).

## 6. Conclusion

As a follow-up of Zubovich et al. (2016) we densified and elongated the western Alai continuous GPS profile and installed the eastern profile to monitor the kinematics of the Pamir thrust system. The improved western profile extends far South into the Trans Alai range and is most densely spaced (~2.5 km) near the surface trace of the Aramkungey fault, a dextral-transpressive fault segment that links two right-stepping thrust segments with opposite dip and unites with the basal décollement of the thin-skinned Pamir thrust system. In addition, survey GPS data were collected over six consecutive years to further densify the network and extend it northward into the South Tien Shan. The Alai GPS network captured co-seismic displacement during and post-seismic rate changes following the 2015 $M_w$7.2 Sarez earthquake. 4-6 years-long, continuous high-rate GPS time-series provide insight in the kinematic response of a fault exposed to a large earthquake occurring at 120–170 km distance. These time-series exhibit co-seismic station offsets of 10–20 mm toward the epicenter of the Sarez earthquake in agreement with its slip mechanism, indicating a slight load decrease of the Pamir frontal thrust. In the western transfer PFT segment, the offsets rapidly decay across $a > 7.5$ km-wide zone around the Aramkungey fault. Further east we observed interferometric offsets of 5–10 mm in line-of-sight tracing a 20–30 km-long, central segment of the PFT. Both observations suggest a co-seismic activation of the PFT during the Sarez earthquake.

Postseismic cGPS rates show that relocking of the Aramkungey fault, unlocked by the Sarez earthquake in a retrograde fashion, began already ~0.5–2.5 years after this event and increased in the following ~2.5–4.5 years, but did not yet reach the full level observed before the earthquake. This is most apparent at the stations closest to the Aramkungey fault, where the profile-parallel and profile-perpendicular post-seismic rate change patterns differ. The front-parallel rates suggest either creep movements along the Aramkungey fault, or initial locking in the upper part. The front-parallel rates indicate a continued accumulation of elastic deformation, slightly reduced by the Sarez event and the following, postseismic processes. The findings are supported by InSAR East rates that, on top, highlight retrograde slip activity on the northernmost fault strands of the Pamir frontal thrust system, again suggesting rather shallow slip.

We rule out a significant kinematic contribution to the north-advance of the Pamir of the thick-skinned structures buried underneath the (western) Alai valley sediments. The major shortening and dextral shear is accommodated by the Pamir thrust system under the Trans Alai range.

The comparison of East and West Alai GPS profile rates confirms that the eastern and western segments of the Pamir thrust system are kinematically decoupled due to the westward escape of the West Pamir. Our study showcases an example of co-seismic retrograde activation of neighboring faults during a large earthquake. At the latest since the well-observed 2019 $M_w$7.1 Ridgecrest earthquake we know that such events evoke complex faulting patterns reaching out to conjugate faults at the boundary between near- and far-field. The implications of this to the overall fault loading states and consequent seismic hazard assessment will be a key question in future research.

## Data Availability Statement

Interferometric data were processed on JASMIN, the UK's collaborative data analysis environment. They are originally based on Copernicus Sentinel data. The cGPS data are archived at Zenodo (https://zenodo.org/record/6555931). Some figures were created using GMT (Wessel et al., 2013) and scientific color maps (Crameri, 2020). The cGPS reference data are made available by the IGS (Johnston et al., 2017). We also would like to thank our colleagues who helped with the installation and maintenance of the ROMPS stations as well as with the data acquisition, namely Julia Illigner, Nico Stolarczuk, Torsten Queisser, Matthias Köppl (all GFZ Potsdam), and Abdysamat Shakirov, Mikhail Borisov, Joldosh Okoev (all CAIAG).

## References

Arrowsmith, J. R., & Strecker, M. R. (1999). Seismotectonic range-front segmentation and mountain-belt growth in the Pamir-Alai region, Kyrgyzstan (India-Eurasia collision zone). *The Geological Society of America Bulletin*, *111*(11), 1665–1683. https://doi.org/10.1130/0016-7606(1999)111<1665:SRFSAM>2.3.CO;2

Avouac, J. P., & Tapponnier, P. (1993). Kinematic model of active deformation in central Asia. *Geophysical Research Letters*, *20*(10), 895–898. https://doi.org/10.1029/93GL00128

Avouac, J. P., Tapponnier, P., Bai, M., You, H., & Wang, G. (1993). Active thrusting and folding along the northern Tien Shan and late Cenozoic rotation of the Tarim relative to Dzungaria and Kazakhstan. *Journal of Geophysical Research*, *98*(B4), 6755–6804. https://doi.org/10.1029/92JB01963

Bloch, W., Metzger, S., Schurr, B., Yuan, X., Ratschbacher, L., Reuter, S., et al. (2021). The 2015–2017 Pamir earthquake sequence: Fore-, main-, and aftershocks, seismotectonics and fault interaction. *Earth and Space Science Open Archive*. https://doi.org/10.1002/essoar.10508392.2

Bürgmann, R., & Dresen, G. (2008). Rheology of the lower crust and upper mantle: Evidence from rock mechanics, geodesy, and field observations. *Annual Review of Earth and Planetary Sciences*, *36*(1), 531–567. https://doi.org/10.1146/annurev.earth.36.031207.124326

Calais, E., Camelbeeck, T., Stein, S., Liu, M., & Craig, T. J. (2016). A new paradigm for large earthquakes in stable continental plate interiors. *Geophysical Research Letters*, *43*(20), 10621–10637. https://doi.org/10.1002/2016GL070815

Chen, S., Tang, L., Jin, Z., Jia, C., & Pi, X. (2004). Thrust and fold tectonics and the role of evaporites in deformation in the Western Kuqa Foreland of Tarim Basin, Northwest China. *Marine and Petroleum Geology*, *21*(8), 1027–1042. https://doi.org/10.1016/j.marpetgeo.2004.01.008

Coutand, I., Strecker, M. R., Arrowsmith, J. R., Hilley, G. E., Thiede, R. C., Korjenkov, A., & Omuraliev, M. (2002). Late Cenozoic tectonic development of the intramontane Alai Valley, (Pamir-Tien Shan region, central Asia): An example of intracontinental deformation due to the Indo-Eurasia collision. *Tectonics*, *21*(6), 1053–3–19. https://doi.org/10.1029/2002TC001358

Crameri, F. (2020). Scientific colour maps (version 6.0.4). https://doi.org/10.5281/zenodo.4153113

Di Giacomo, D. D. I., Bondár, I., Storchak, D. A., Engdahl, E. R., Bormann, P., & Harris, J. (2015). ISC-GEM: Global Instrumental Earthquake Catalogue (1900–2009): III. Re-computed MS and mb, proxy MW, final magnitude composition and completeness assessment. *Physics Earth Planetary Interiors*, *239*, 33–47. https://doi.org/10.1016/j.pepi.2014.06.005

Elliott, J. R., Jolivet, R., Gonzalez, P. J., Avouac, J. P., Hollingsworth, J., Searle, M. P., & Stevens, V. L. (2016). Himalayan megathrust geometry and relation to topography revealed by the Gorkha earthquake. *Nature Geoscience*, *9*(2), 174–180. https://doi.org/10.1038/ngeo2623

Evans, S. G., Nicholas, J. R., Ischuk, A., Delaney, K. B., Morozova, G. S., & Tutubalina, O. (2009). Landslides triggered by the 1949 Khait earthquake, Tajikistan, and associated loss of life. *Engineering Geology*, *109*(3–4), 195–212. https://doi.org/10.1016/j.enggeo.2009.08.007

Feng, W., Tian, Y., Zhang, Y., Samsonov, S., Almeida, R., & Liu, P. (2017). A slip gap of the 2016 $M_w$6.6 Muji, Xinjiang, China, earthquake inferred from Sentinel-1 TOPS interferometry. *Seismological Research Letters*, *88*(4), 1054–1064. https://doi.org/10.1785/0220170019

Fialko, Y., Sandwell, D., Agnew, D., Simons, M., Shearer, P., & Minster, B. (2002). Deformation on nearby faults induced by the 1999 Hector Mine earthquake. *Science*, *297*(5588), 1858–1862. https://doi.org/10.1126/science.1074671

Funning, G. J., & Garcia, A. (2019). A systematic study of earthquake detectability using Sentinel-1 Interferometric Wide-Swath Data. *Geophysical Journal International*, *216*(1), 332–349. Figure S23, supplementary material. https://doi.org/10.1093/gji/ggy426

Geirsson, H., Árnadóttir, T., Völksen, C., Jiang, W., Sturkell, E., Villemin, T., et al. (2006). Current plate movements across the Mid-Atlantic Ridge determined from 5 years of continuous GPS measurements in Iceland. *Journal of Geophysical Research*, *111*(B9), B09407. https://doi.org/10.1029/2005JB003717

GEOFON Data Centre. (2006). *Moment tensor solution for the 2016 $M_w$6.4 Sary-Tash, Kyrgyzstan earthquake*. GFZ German Research Centre for Geosciences. Retrieved from http://geofon.gfz-potsdam.de/eqinfo/event.php?id=gfz2016mmgj

Gubin, I. E. (1940). Geological boundary between Pamir and Alai, M.-L. (Gosgeolizdat) (p. 48).

Hamburger, M. W., Sarewitz, D. R., Pavlis, T. L., & Popandopulo, G. A. (1992). Structural and seismic evidence for intracontinental subduction in the peter the first range, central Asia. *The Geological Society of America Bulletin*, *104*(4), 397–408. https://doi.org/10.1130/0016-7606

Herring, T. A., Floyd, M. A., King, R. W., & McClusky, S. C. (2015). *GLOBK reference manual, Global Kalman filter VLBI and GPS analysis program, release 10.6*. Department of Earth, Atmospheric, and Planetary Sciences Massachusetts Institute of Technology.

Herring, T. A., King, R. W., Floyd, M. A., & McClusky, S. C. (2018). *GAMIT reference manual, reference GPS analysis at MIT, release 10.7*. Department of Earth, Atmospheric, and Planetary Sciences, Massachusetts Institute of Technology.

Herring, T. A., King, R. W., & McClusky, S. C. (2009). *Introduction to GAMIT/GLOBK, release 10.35*. Massachusetts Institute of Technology.

Hooper, A., Segall, P., & Zebker, H. (2007). Persistent scatterer interferometric synthetic aperture radar for crustal deformation analysis, with application to Volcán Alcedo, Galápagos. *Journal of Geophysical Research: Solid Earth*, *112*(7), 1–21. https://doi.org/10.1029/2006JB004763

Hubbard, J., & Shaw, J. H. (2009). Uplift of the Longmen Shan and Tibetan plateau, and the 2008 Wenchuan ($M = 7.9$) earthquake. *Nature*, *458*(7235), 194–197. https://doi.org/10.1038/nature07837

Ischuk, A., Bendick, R., Rybin, A., Molnar, P., Khan, S. F., Kuzikov, S., et al. (2013). Kinematics of the Pamir and Hindu Kush regions from GPS geodesy. *Journal of Geophysical Research: Solid Earth*, *118*(5), 2408–2416. https://doi.org/10.1002/jgrb.50185

Jin, Z., Fialko, Y., Zubovich, A., & Schöne, T. (2022). Lithospheric deformation due to the 2015 M7.2 Sarez (Pamir) earthquake constrained by 5 years of space geodetic observations. *Journal of Geophysical Research: Solid Earth*, *127*(4), e2021JB022461. https://doi.org/10.1029/2021JB022461

Johnston, G., Riddell, A., & Hausler, G. (2017). The International GNSS Service. In P. J. G. Teunissen & O. Montenbruck (Eds.), *Springer handbook of global navigation satellite systems* (1st ed., pp. 967–982). Springer International Publishing. https://doi.org/10.1007/978-3-319-42928-1

Jónsson, S., Segall, P., Pedersen, R., & Björnsson, G. (2003). Post-earthquake ground movements correlated to pore-pressure transients. *Nature Geoscience*, *424*(6945), 179–183. https://doi.org/10.1038/nature0177

Kulikova, G. (2016). *Source parameters of the major historical earthquakes in the Tien-Shan region from the late 19th to the early 20th century, PhD Thesis*. Potsdam University. Retrieved from https://publishup.uni-potsdam.de/opus4-ubp/frontdoor/deliver/index/docId/8837/file/kulikova_diss.pdf

Kulikova, G., & Krüger, F. (2015). Source process of the 1911 M8.0 Chon-Kemin earthquake: Investigation results by analogue seismic records. *Geophysical Journal International*, *3*, 1891–1911. https://doi.org/10.1093/gji/ggv091

Kulikova, G., Schurr, B., Krüger, F., Brzoska, E., & Heimann, S. (2016). Source parameters of the Sarez-pamir earthquake of 1911 February 18. *Geophysical Journal International*, *205*(2), 1086–1098. https://doi.org/10.1093/gji/ggw069

Lazeckỳ, M., Spaans, K., González, P. J., Maghsoudi, Y., Morishita, Y., Albino, F., et al. (2020). LiCSAR: An automatic InSAR tool for measuring and monitoring tectonic and volcanic activity. *Remote Sensing*, *12*(15), 2430. https://doi.org/10.3390/RS12152430

Li, T., Schoenbohm, L. M., Chen, J., Yuan, Z., Feng, W., Li, W., et al. (2019). Cumulative and coseismic (during the 2016 $M_w$ 6.6 Aketao earthquake) deformation of the dextral-slip Muji Fault, northeastern Pamir orogen. *Tectonics*, *38*(11), 3975–3989. https://doi.org/10.1029/2019TC005680

Marone, C. J., Scholtz, C. H., & Bilham, R. (1991). On the mechanics of earthquake afterslip. *Journal of Geophysical Research*, *96*(B5), 8441–8452. https://doi.org/10.1029/91JB00275

Metzger, S., Gągała, Ł., Ratschbacher, L., Schurr, B., Lazecky, M., & Maghsoudi, Y. (2021). Tajik depression and greater Pamir neotectonics from InSAR rate maps. *Journal of Geophysical Research: Solid Earth*, *126*(12), e2021JB022775. https://doi.org/10.1029/2021JB022775

Metzger, S., Ischuk, A., Deng, Z., Ratschbacher, L., Perry, M., Kufner, S. K., et al. (2020). Dense GNSS profiles across the northwestern tip of the India-Asia collision zone: Triggered slip and westward flow of the Peter the First Range, Pamir, into the Tajik Depression. *Tectonics*, *39*, e2019TC005797. https://doi.org/10.1029/2019TC005797

Metzger, S., Jónsson, S., Danielsen, G. J. K., Hreinsdottir, S., Jouanne, F., Giardini, D., & Villemin, T. (2013). Present kinematics of the Tjörnes Fracture Zone, North Iceland, from campaign and continuous GPS measurements. *Geophysical Journal International*, *192*(2), 441–455. https://doi.org/10.1093/gji/ggs032

Metzger, S., Kakar, N., Zubovich, A., Borisov, M., Saif, S., Panjsheri, A. H., et al. (2021). *Survey mode GNSS data, acquired 2014–2019 in the Afghan Hindu Kush and across northern Pamir margin, Central Asia*. GFZ Data Services. https://doi.org/10.5880/GFZ.4.1.2021.003

Metzger, S., Lazecky, M., & Maghsoudi, Y. (2021). *High-resolution rate maps from the Tajik basin and the Pamir*. GFZ Data Services. https://doi.org/10.5880/GFZ.4.1.2021.005

Metzger, S., Schurr, B., Ratschbacher, L., Sudhaus, H., Kufner, S.-K., Schöne, T., et al. (2017). The 2015 $M_w$7.2 Sarez strike-slip earthquake in the Pamir interior: Response to the underthrusting of India's western promontory. *Tectonics*, *36*(11), 2407–2421. https://doi.org/10.1002/2017TC004581

Mohadjer, S., Bendick, S. R., Ischuk, A., Kuzikov, S., Kostuk, A., Saydullaev, U., et al. (2010). Partitioning of India/Eurasia convergence in the Pamir-Hindu Kush from GPS measurements. *Geophysical Research Letters*, *37*(4), L04305. https://doi.org/10.1029/2009GL041737

Mohadjer, S., Ehlers, T. A., Bendick, R., Stübner, K., & Strube, T. (2016). A quaternary fault database for central Asia. *Natural Hazards and Earth System Sciences*, *16*(2), 529–542. https://doi.org/10.5194/nhess-16-529-2016

Morishita, Y., Lazecky, M., Wright, T. J., Weiss, J. R., Hooper, A., Elliott, J. R., & Hooper, A. (2020). LiCSBAS: An open-Source InSAR time series analysis package integrated with the LiCSAR automated Sentinel-1 InSAR processor. *Remote Sensing*, *12*(3), 5–8. https://doi.org/10.3390/rs12030424

Nikonov, A. A. (1988). Reconstruction of the main parameters of old large earthquakes in Soviet Central Asia using the paleoseismogeological method. *Tectonophysics*, *147*(3–4), 297–312. https://doi.org/10.1016/0040-1951(88)90191-6

Nur, A., & Mavko, G. (1974). Postseismic viscoelastic rebound. *Science*, *183*(4121), 204–206. https://doi.org/10.1126/science.183.4121.204

Ou, Q. (2020). *Crustal deformation and seismic hazard of the NE Tibetan Plateau, PhD Thesis*. University of Oxford.

Patyniak, M., Landgraf, A., Dzhumabaeva, A., Baikulov, S., Williams, A. M., Weiss, J. R., et al. (2021). The Pamir Frontal Thrust fault: Holocene full-segment ruptures and implications for complex segment interactions in a continental collision zone. *Journal of Geophysical Research: Solid Earth*, *126*(12), e2021JB022405. https://doi.org/10.1029/2021JB022405

Peltzer, G., Rosen, P., Rogez, F., & Hudnut, K. (1998). Poroelastic rebound along the Landers 1992 earthquake surface rupture. *Journal of Geophysical Research*, *103*(B12), 30131–30145. https://doi.org/10.1029/98JB02302

Perfettini, H., Avouac, J.-P., Tavera, H., Kositsky, A., Nocquet, J.-M., Bondoux, F., et al. (2010). Seismic and aseismic slip on the Central Peru megathrust. *Nature*, *465*(7294), 78–81. https://doi.org/10.1038/nature09062

Ramos, M. D., Neo, J. C., Thakur, P., Huang, Y., & Wei, S. (2020). Stress changes on the Garlock fault during and after the 2019 ridgecrest earthquake sequence. *Bulletin of the Seismological Society of America*, *110*(4), 1752–1764. https://doi.org/10.1785/0120200027

Reigber, C., Michel, G. W., Galas, R., Angermann, D., Klotz, J., Chen, J. Y., et al. (2001). New space geodetic constraints on the distribution of deformation in Central Asia. *Earth and Planetary Science Letters*, *191*(1–2), 157–165. https://doi.org/10.1016/S0012-821X(01)00414-9

Sangha, S., Peltzer, G., Zhanga, A., Menga, L., Liang, C., Lundgren, P., & Fielding, E. (2017). Fault geometry of 2015, $M_w$7. 2 Murghab, Tajikistan earthquake controls rupture propagation: Insights from InSAR and seismological data. *Earth and Planetary Science Letters*, *462*, 132–141. https://doi.org/10.1016/j.epsl.2017.01.018

Savage, J. C., & Burford, R. O. (1973). Geodetic determination of relative plate motion in central California. *Journal of Geophysical Research*, *78*(5), 832–845. https://doi.org/10.1029/JB078i005p00832

Schöne, T., Zech, C., Unger-Shayesteh, K., Rudenko, V., Thoss, H., Wetzel, H.-U., et al. (2013). A new permanent multi-parameter monitoring network in Central Asian high mountains—From measurements to data bases. *Geoscientific Instrumentation, Methods and Data Systems*, *2*, 97–111. https://doi.org/10.5194/gid-2-301-2012

Schurr, B., Ratschbacher, L., Sippl, C., Gloaguen, R., Yuan, X., & Mechie, J. (2014). Seismotectonics of the Pamir. *Tectonics*, *33*(8), 1501–1518. https://doi.org/10.1002/2014TC003576

Sippl, C., Ratschbacher, L., Schurr, B., Krumbiegel, C., Rui, H., Pingren, L., & Abdybachaev, U. (2014). The 2008 Nura earthquake sequence at the Pamir-Tian Shan collision zone, southern Kyrgyzstan. *Tectonics*, *33*(12), 2382–2399. https://doi.org/10.1002/2014TC003705

Sobel, E., & Dumitru, T. (1997). Thrusting and exhumation around the margins of the western Tarim basin during the India-Asia collision. *Journal of Geophysical Research*, *102*(B3), 5043–5063. https://doi.org/10.1029/96JB03267

Strecker, M. R., Frisch, W., Hamburger, M. W., Ratschbacher, L., Semiletkin, S., Zamoruyev, A., & Sturchio, N. (1995). Quaternary deformation in the eastern Pamirs, Tadzhikistan and Kyrgyzstan. *Tectonics*, *14*(5), 1061–1079. https://doi.org/10.1029/95TC00927

Strecker, M. R., Hilley, G. E., Arrowsmith, J. R., & Coutand, I. (2003). Differential structural and geomorphic mountain-front evolution in an active continental collision zone: The northwest Pamir, southern Kyrgyzstan. *The Geological Society of America Bulletin*, *115*(2), 166–181. https://doi.org/10.1130/0016-7606(2003)115<0166:DSAGMF>2.0.CO;2

Teshebaeva, K., Sudhaus, H., Echtler, H., Schurr, B., & Roessner, S. (2014). Strain partitioning at the eastern Pamir-Alai revealed through SAR data analysis of the 2008 Nura earthquake. *Geophysical Journal International*, *198*(2), 760–774. https://doi.org/10.1093/gji/ggu158

Vajedian, S., Motagh, M., Wetzel, H.-U., & Teshebaeva, K. (2017). Coupling of Sentinel-1, Sentinel-2 and ALOS-2 to assess coseismic deformation and earthquake-induced landslides following the 26 June, 2016 earthquake in Kyrgyzstan. *Geophysical Research Abstracts*, *19*, EGU2017-18464-1. https://meetingorganizer.copernicus.org/EGU2017/EGU2017-18259.pdf

van Hinsbergen, D. J., Lippert, P. C., Dupont-Nivet, G., McQuarrie, N., Doubrovine, P. V., Spakman, W., & Torsvik, T. H. (2012). Greater India Basin hypothesis and a two-stage Cenozoic collision between India and Asia. *Proceedings of the National Academy of Sciences*, *109*(20), 7659–7664. https://doi.org/10.1073/pnas.1117262109

Velasco, A. A., Hernandez, S., Parsons, T., & Pankow, K. (2008). Global ubiquity of dynamic earthquake triggering. *Nature Geoscience*, *1*(6), 375–379. https://doi.org/10.1038/ngeo204

Voigt, T., Kley, J., & Wehner, C. (2020). A mountain of folds: Triangle zone in the fold-and-thrust belt of the external Pamir, Kyrgyzstan. EGU General Assembly, EGU2020-22109. https://doi.org/10.5194/egusphere-egu2020-22109

Wang, K., Hu, Y., & He, J. (2012). Deformation cycles of subduction earthquakes in a viscoelastic Earth. *Nature*, *484*(7394), 327–332. https://doi.org/10.1038/nature11032

Wang, S., Xu, C., Wen, Y., Yin, Z., Jiang, G., & Fang, L. (2017). Slip model for the 25 November 2016 $M_w$6.6 Aketao earthquake, Western China, revealed by Sentinel-1 and ALOS-2 observations. *Remote Sensing*, *9*(4), 325. https://doi.org/10.3390/rs9040325

Wdowinski, S., Bock, Y., Zhang, J., Fang, P., & Genrich, J. (1997). Southern California permanent GPS geodetic array: Spatial filtering of daily positions for estimating coseismic and postseismic displacements induced by the 1992 Landers earthquake. *Journal of Geophysical Research: Solid Earth*, *102*(B8), 18057–18070. https://doi.org/10.1029/97JB01378

Wessel, P., Smith, W. H. F., Scharroo, R., Luis, J. F., & Wobbe, F. (2013). Generic mapping Tools: Improved version released. *Eos, Transactions American Geophysical Union*, *94*(45), 409–410. https://doi.org/10.1002/2013EO450001

Wright, T., Fielding, E. J., & Parsons, B. (2001). Triggered slip: Observations of the 17 August 1999 Izmit (Turkey) earthquake using radar interferometry. *Geophysical Research Letters*, *28*(6), 1079–1082. https://doi.org/10.1029/2000GL011776

Xu, X., Sandwell, D. T., & Smith-Konter, B. (2020). Coseismic displacements and surface fractures from Sentinel-1 InSAR: 2019 ridgecrest earthquakes. *Seismological Research Letters*, *91*(4), 1997–1985. https://doi.org/10.1785/0220190275

Yu, C., Li, Z., Penna, N. T., & Crippa, P. (2018). Generic atmospheric correction model for interferometric synthetic aperture radar observations. *Journal of Geophysical Research: Solid Earth*, *123*(10), 9202–9222. https://doi.org/10.1029/2017JB015305

Zaalaian Exploration Team. (1993). Geological structure and minerals of Alai area. Report on exploration works of a 1:50,000 scale in the area of the sheets J-43-3-А-г, Б, В, Г, J-43-14-А, Б-а, б, Г, J-43-15-А, Б, В, 1987–1993.

Zech, C., Schöne, T., Illigner, J., Stolarczuk, N., Queißer, T., Köppl, M., et al. (2021). Hydrometeorological data from a remotely operated multi-parameter station network in central Asia. *Earth System Science Data*, *13*(3), 1289–1306. https://doi.org/10.5194/essd-13-1289-2021

Zubovich, A. V., Schöne, T., Metzger, S., Mosienko, O., Mukhamediev, S., Sharshebaev, A., & Zech, C. (2016). Tectonic interaction between the Pamir and Tien Shan observed by GPS. *Tectonics*, *35*(2), 283–292. https://doi.org/10.1002/2015TC004055

Zubovich, A. V., Wang, X. Q., Scherba, Y. G., Schelochkov, G. G., Reilinger, R., Reigber, C., et al. (2010). GPS velocity field of the Tien Shan and surrounding regions. *Tectonics*, *29*(TC6014), 1–23. https://doi.org/10.1029/2010TC002772